Fatigue damage characterisation of MarBN steel for high temperature flexible operating conditions

Fatigue Damage Characterisation of MarBN Steel for High Temperature Flexible Operating Conditions

E.M. O'Hara[1,2], N.M. Harrison[1,2], B.K. Polomski[3], R.A. Barrett[1,2], S.B. Leen[1,2]

[1]Mechanical Engineering, College of Engineering & Informatics, NUI Galway, H91 HX31, Ireland

[2]Ryan Institute for Environmental, Marine and Energy Research, NUI Galway, H91 HX31, Ireland

[3]GE Power, Gas Power Systems, Newbold Road, Rugby, Warwickshire, CV21 2NH, United Kingdom

Abstract

This paper is concerned with the high temperature low cycle fatigue behaviour of a new nano-strengthened martensitic-ferritic steel, MarBN. A range of strain-controlled, low cycle fatigue tests are presented on MarBN at 600 °C and 650 °C, and compared with previously published data for a current state-of-the-art material, P91 steel, including microstructural analysis of the fracture mechanisms. A modified Chaboche damage law, incorporating Coffin-Manson life prediction, is implemented within a hyperbolic sine unified cyclic viscoplastic constitutive model. Calibration and validation of the model with respect to the effects of strain-rate and strain-range is performed based on an optimisation procedure for identification of the material parameters. The cyclic viscoplasticity model with damage successfully predicts fatigue damage evolution and life in the cyclically-softening materials, MarBN and P91.

Keywords: 9Cr steels, fatigue, damage, life prediction, high temperature low cycle fatigue, mechanisms of deformation

1. Introduction

The world faces a significant challenge to meet the requirements of providing cost-effective, abundant electricity for a growing population, whilst also ensuring minimal environmental impact. Improved efficiency of power plants is key to reducing emissions and cost through the implementation of advanced steam cycles [1–3]. Due to the intermittent nature of renewable energy sources, existing power plants, designed for base-load operation, must adopt a load-following mode, leading to an increased frequency of start-up and shut-down cycles [2,4,5]. Such complex operational cycles will cause increased thermo-mechanical fatigue (TMF) and creep-fatigue (CF) of components and hence, increase the risk of component failure [6–8]. Thus, multi-scale characterisation of advanced high temperature next generation materials is necessary to accurately demonstrate material degradation during service life [4,5,9]. 9Cr steels have been developed as a cost-effective alternative to nickel-based superalloys, but need to be investigated for flexible operation at higher temperatures and pressures [10].

Alloy development of advanced ferritic steels has shown that the addition of vanadium, niobium and nitrogen can increase creep strength and chromium can provide increased oxidation resistance at higher temperatures. The characterising feature of 9Cr steels is a tempered martensitic lath structure which contains $M_{23}C_6$ (M = Fe, Cr, Mo, W) carbides and MX (VN, NbC) type carbonitrides. High dislocation density and a fine lath structure are key features of 9Cr martensitic-ferritic steels. The hierarchical microstructure of 9Cr steels, as presented in Figure 1 [11], consists of prior austenite grains, packets and blocks. These blocks are divided into laths and subgrain regions demarcated by dislocation arrays constituting low angle boundaries [6,12,13]. The densely distributed dislocation substructure opposes dislocation motion and increases resistance to plastic deformation. The addition of small controlled amounts of nitrogen produces a fine MX particle dispersion throughout the microstructure and allows prior-austenitic grain growth during normalizing, as part of a two-step normalising and tempering heat treatment process, resulting in significantly larger grain sizes than other ferritic steels [13–15]. Literature has shown that the addition of boron to 9Cr steels can promote a more refined precipitate distribution compared to materials such as P91 and reduce the rate of

coarsening at high temperature due to its distribution within the $M_{23}C_6$ grain boundary carbides [13,15]. To maintain the fine lath structure pinning by $M_{23}C_6$ and MX particles and solute atoms (W, Co) is necessary due to the large driving force for recovery as a result of the high dislocation density. The addition of tungsten is found to reduce initial lath size, and combined with boron, delay carbide coarsening, which is found to occur over temperatures of 550 °C, hence retaining the fine grained substructure for longer [6,12].

For both high temperature creep and fatigue loading conditions, the microstructure of 9Cr steel is found to exhibit lath and subgrain coarsening leading to cyclic softening behaviour [3,16–19]. High temperature cyclic softening is found to generally occur in materials with a high dislocation density and leads to loss of strength in 9Cr steels. The physical mechanisms have been identified as (i) loss of low angle boundary (LAB) dislocations and hence (ii) decrease in overall dislocation density and coarsening of the lath structure, and (iii) precipitate coarsening [6]. An experimental program of high temperature low cycle fatigue (HTLCF) and stress relaxation (SR) testing on MarBN at 600 °C has shown a significant cyclic softening effect, but an increased stress range in the material, when compared to P91 steel at 600 °C [20]. MarBN has shown superior creep resistance at elevated temperatures, when compared to current generation materials, such as P91, P92 and P122, with potential for future applications at ultra-supercritical temperatures and pressures [13,21].

Fatigue damage in metals is primarily attributed to irreversible plastic deformation, generally as a result of dislocation motion, and is dependent on factors such as precipitates, inclusions and grain boundaries in the material [22,23]. At an early stage of fatigue loading, microstructural changes occur in the bulk of the material under cyclic loading whereby irreversible dislocation movement occurs [22]. Plastic deformation of ductile materials can cause decohesion of the particle-matrix interface or fracture of inclusions, leading to microvoid growth and microcrack initiation at elevated temperatures. Decohesion or inclusion fracture primarily results from stress concentrations, due to dislocation pile-up at inclusions, for example [23–27].

The concept of a damage parameter was first introduced by Kachanov [28]. Rabotnov [29] introduced an effective stress concept for a material under tensile loading, based on the growth of microdefects.

With respect to simulating fatigue damage, a relatively large number of models exist. The work of Lemaitre [30] describes damage based on plastic strain, Chaboche [31] defined a simple cumulative fatigue damage model based on number of cycles to failure, a damage criterion based on total strain energy per cycle was implemented by Golos [32], and Cheng [33] proposed a fatigue damage model based on ductility exhaustion and continuum damage mechanics, for example. The interaction between creep and fatigue loading has also been investigated using a number of approaches, including strain range partitioning and linear damage summation [34–37]. A key challenge for the case of 9Cr steels, which cyclically soften due to microstructure evolution, is the identification of fatigue damage evolution for prediction of crack initiation and hence failure.

The objective of this work is to present a low-cycle fatigue damage evolution model for MarBN and P91 under HTLCF conditions. This paper presents results for MarBN at 600 °C and 650 °C, as well as P91 at 500 °C and 600 °C, including the effects of strain-rate and strain-range. Fractography is presented to illustrate the damage mechanisms in MarBN post-test and the role of inclusions is also investigated. A variation of the Chaboche [31] damage law, incorporating Coffin-Manson [38] life prediction is implemented in a hyperbolic sine unified cyclic viscoplastic material model. An optimisation procedure has also been developed to increase accuracy of prediction of material response. A Chaboche non-linear isotropic softening model is employed to identify the onset of crack initiation. For subsequent cycles, both cyclic softening and fatigue accumulation are assumed to contribute to material degradation and hence failure. This new approach is applied to the MarBN and P91 materials and conditions for prediction of crack initiation.

2. Materials & Methods

2.1. Experimental Testing

The current generation of power plants operate at temperatures up to 600 °C; however, future plants must increase operating temperatures up to 650 °C and above to achieve increased efficiency, highlighting the key limitation of suitable materials capable of operating under such conditions. Therefore fully reversed (triangular) HTLCF testing is performed on a MarBN material at 600 °C and 650 °C using the strain-controlled test rig at NUI Galway, shown in Figure 2. This expands on the

previously published test program by Barrett et al. [20], which conducted a program of HTLCF and SR testing on MarBN at 600 °C, as shown in Table 1. The failure criterion is a 20% drop in load after the first 150 cycles of testing. The grade of MarBN tested is a cast material, which has been developed as part of the industry–academic UK project IMPEL [39], and using a similar heat treatment process to Li et al. [13].

2.2. Microstructural Analysis

Microstructural analysis is performed on samples, both pre- and post-test. The samples are set in resin and polished, using a Buehler EcoMet 300 with Automet 250, to a 0.06 μm finish and etched with Vilella's reagent. Scanning electron microscopy (SEM) and energy-dispersive X-ray spectroscopy (EDX) analysis is performed using the Hitachi S-4700 SEM with EDX at NUI Galway.

2.3. Material Model

The material model is an extension of a hyperbolic sine unified cyclic viscoplastic material model [9], to incorporate life prediction and damage accumulation. A key aspect of the model is the use of strain-rate independent material parameters due to the significant strain-rate effect observed in 9Cr steels above 500 °C. Alternative approaches employ uncoupled creep and plastic strain and this is convenient for application of the strain-range partitioning method [35], for example. However, the unified approach is more generally applicable to combined cyclic fatigue and creep conditions [7] and, more importantly, permits more reliable extrapolation and interpolation to the lower strain-rates observed during power plant operation based on a relatively small amount of laboratory testing [9]. The model calculates the number of cycles to failure and damage simultaneously, based on a set of optimised material parameters for MarBN and also P91. The plastic strain-rate, $\dot{\varepsilon}^{\mathrm{pl}}$, is defined as:

$$\dot{\varepsilon}^{\mathrm{pl}} = \alpha \sinh \beta\left(\left|\tilde{\sigma} - \chi\right| - R - k\right)\mathrm{sgn}\left(\tilde{\sigma} - \chi\right) \tag{1}$$

where α and β are the viscoplastic material constants, $\tilde{\sigma}$ is the effective stress, the χ term accounts for the Bauschinger effect, isotropic softening behaviour is described by the R term, and k is initial yield stress. Damage is included in the model via the effective stress, as follows:

$$\tilde{\sigma} = \frac{\sigma}{(1-D)} \tag{2}$$

where σ is the stress, and D is damage. The initial and later strain hardening stages are described through the use of two hardening terms in the kinematic hardening evolution model of Armstrong-Frederick, such that $\chi = \chi_1 + \chi_2$. The evolutionary equation for the Armstrong-Frederick model is:

$$\dot{\chi}_{\mathrm{i}} = C_{\mathrm{i}}\dot{\varepsilon}^{\mathrm{pl}}(1-D) - \gamma_{\mathrm{i}}\chi_{\mathrm{i}}\dot{p} \tag{3}$$

where C_{i} is the hardening modulus, γ_{i} is a recall parameter and $\dot{p}$ is the accumulated plastic strain-rate. Two Chaboche [40,41] isotropic softening terms are used to simulate the primary and secondary stages of softening, such that $R = R_1 + R_2$ [20]. The evolution of R is defined as follows:

$$\dot{R}_{\mathrm{i}} = b_{\mathrm{i}}Q_{\mathrm{i}}(1-D)\dot{p} - b_{\mathrm{i}}R_{\mathrm{i}}\dot{p} \tag{4}$$

where the rate of decay is controlled by b_{i} and Q_{i} is the saturated cyclic softening stress. In the present work which is initially focused on uniaxial fatigue behaviour, fatigue damage is defined here using the model of Chaboche [31]:

$$D = 1 - \left[1 - \left(\frac{N}{N_{\mathrm{f}}}\right)^{\frac{1}{1-\phi_1}}\right]^{\frac{1}{\phi_2 - 1}} \tag{5}$$

where N is cycle number, ϕ_1 and ϕ_2 are damage constants and N_{f} is number of cycles to failure, defined using the Coffin-Manson [38] model for low-cycle fatigue:

$$\frac{\Delta\varepsilon^{\mathrm{pl}}}{2} = \varepsilon_{\mathrm{f}}^{'}\left(2N_{\mathrm{f}}\right)^{\mathrm{c}} \tag{6}$$

where $\varepsilon_{\mathrm{f}}^{'}$ and c are the fatigue ductility coefficient and exponent, respectively. Differentiation of Equation (5), with respect to number of cycles, gives an equation for the damage rate, as follows:

$$\frac{dD}{dN} = \left[\left(\frac{1}{1-\phi_2}\right)\left(1 - \left(\frac{N}{N_{\mathrm{f}}(N)}\right)^{\frac{1}{1-\phi_1}}\right)^{\frac{2-\phi_2}{\phi_2-1}}\right]\left[\left(\frac{1}{\phi_1 - 1}\right)\left(\frac{N}{N_{\mathrm{f}}(N)}\right)^{\frac{\phi_1}{1-\phi_1}}\right]\left[N_{\mathrm{f}}(N) - N\left(\frac{1}{2c\left(2\varepsilon_{\mathrm{f}}^{'}\right)^{\frac{1}{c}}}\Delta\varepsilon^{\mathrm{pl}\frac{1-c}{c}}\frac{\mathrm{d}\Delta\varepsilon^{\mathrm{pl}}}{\mathrm{dN}}\right)\right]\left[N_f(N)\right]^{-2} \tag{7}$$

This material model is implemented in uniaxial form in MATLAB. The unified viscoplastic constitutive model used here has been previously applied to multiaxial conditions, without damage

and life prediction [7]; the present more advanced life prediction model will be applied to multiaxial applications in future work.

2.4. Identification of Material Parameters

The material model, including damage, contains 16 material parameters, which can be classified as follows: (i) elastic, (ii) isotropic softening and kinematic hardening, (iii) cyclic viscoplastic and (iv) damage. The process by which the elastic, isotropic softening and kinematic hardening, and cyclic viscoplastic material parameters are identified is described in detail by Barrett et al. [20]. Young's Modulus, E, and the initial cyclic yield stress, k, are determined from the initial stress-strain cycle. The Chaboche isotropic softening model [40,41] is implemented incorporating two isotropic softening terms to describe the primary and secondary softening behaviour, characteristic of 9Cr steels [9]. The material parameters are identified by integrating Equation (4) and fitting this model to experimental data using a least squares method, as illustrated in Figure 3(a). The kinematic hardening constants are identified by dividing the stress into its various components, such that:

$$\sigma = \chi + \left(R + k + \sigma_v\right)\mathrm{sgn}\left(\sigma - \chi\right) \tag{8}$$

where σ_v is the viscous stress. Differentiation of Equation (8) with respect to plastic strain gives:

$$\ln\left(\frac{\delta\sigma}{\delta\varepsilon^{\mathrm{pl}}} - \frac{\delta R}{\delta\varepsilon^{\mathrm{pl}}}\right) = \ln\left(C_i\right) - \gamma_i\varepsilon^{\mathrm{pl}} \tag{9}$$

where calculation of $\delta\sigma/\delta\varepsilon^{\mathrm{pl}}$ is performed using a Ramberg-Osgood smoothing function. The kinematic hardening constants are then identified by plotting (i) $\ln(\delta\sigma/\delta\varepsilon^{\mathrm{pl}} - \delta R/\delta\varepsilon^{\mathrm{pl}})$ for the later stages of strain hardening, and (ii) $\ln(\delta\sigma/\delta\varepsilon^{\mathrm{pl}} - \delta R/\delta\varepsilon^{\mathrm{pl}} - \delta\chi_2/\delta\varepsilon^{\mathrm{pl}})$ for the initial stages of strain hardening, against $\varepsilon^{\mathrm{pl}}$. The viscoplastic material parameters α and β are identified using an analytical model for stress as a function of time during a dwell period:

$$\sigma = \frac{2}{\beta}\tanh^{-1}\left(\tanh\left(\frac{\beta\left(\sigma_0 - \chi - k\right)}{2}\right)e^{-\alpha\beta E\left(t - t_0\right)}\right) + \chi + k \tag{10}$$

where t_0 and σ_0 are the time and stress at which the hold period begins.

To separate cyclic softening and damage in 9Cr steels a modified damage term is developed:

$$D_{\text{exp}} = 1 - \frac{Z}{Z_0} \tag{11}$$

where

$$Z = \sigma_{\max}(N) - R(N) \tag{12}$$

and $\sigma_{\max}$ is the maximum tensile stress per cycle and Z_0 is the maximum value of Z, as illustrated in Figure 3(b). The parameter Z is defined as the maximum stress minus the microstructurally induced softening stress, R. The assumption in this model is that softening consists of (i) microstructurally induced softening (such as low angle boundary annihilation and particle coarsening) represented by R and (ii) fatigue damage induced softening represented by Z. The Coffin-Manson constants, $\varepsilon_{\text{f}}^{'}$ and c, are determined from the measured plastic strain-range data, $\Delta\varepsilon^{\text{pl}}/2$, at half-life and corresponding numbers of reversals to failure, as shown in Figure 4. The Chaboche damage constants, ϕ_1 and ϕ_2, are identified from the experimentally measured evolution of damage, D_{exp}, with number of cycles, N, via a least squares fitting procedure. The fatigue damage constants for MarBN and P91 are presented in Table 2.

2.5. Optimisation

A flowchart of the material parameter optimisation process, in conjunction with the uniaxial hyperbolic sine cyclic viscoplastic material model, is shown in Figure 5. To increase the accuracy of the material model, and reduce the error between the model and the experimental data, an optimisation procedure is developed using MATLAB for the present viscoplasticity model and applied to MarBN at 600 °C. The initial user estimates to the optimisation function consists of the set of material parameters identified as described in Section 2.4 i.e. the initial yield stress, isotropic softening, kinematic hardening and cyclic viscoplastic material parameters. The optimisation procedure is performed using the Levenberg-Marquardt algorithm, as part of the *lsqnonlin* function in MATLAB. The function optimises an array, x_0, of user-defined constants to fit a range of experimental data by minimising the error between the predicted results and experimental data. The

experimental data consists of stress relaxation and fatigue data, similar to the data required for the original parameter identification method.

3. Results

3.1. Experimental

Figure 4 compares the fatigue life of MarBN at 600 °C and P91 at 500 °C and 600 °C. The cast MarBN is found to have a lower low-cycle fatigue life than P91. Figure 6 shows a comparison between measured stress-strain hysteresis loops for the initial, half-life and final cycles for MarBN at 600 °C and 650 °C and P91 at 600 °C, at a strain-rate of 0.1 %/s and strain-range of ±0.5%. Figure 7 shows the corresponding measured rates of softening for each material and temperature. MarBN at 650 °C exhibits a significantly higher rate of softening than P91 at 600 °C for the duration of testing. MarBN at 600 °C also has a higher rate of softening than P91, even though it exhibits a higher strength prior to the onset of fatigue damage.

3.2. Microstructural Analysis

SEM images of MarBN in the as-received condition and post-HTLCF testing at 600 °C are presented in Figure 8, with a comparison to P91 post-HTLCF test at 600 °C. Grain boundaries are highlighted for comparison between MarBN and P91, and a significantly larger grain size is observed in the cast MarBN compared to the rolled P91. Ductile dimples are observed on the fracture surface of MarBN test samples post-HTLCF testing (Figure 9), which have been found to occur due to microvoid coalescence and growth at inclusions as a result of fatigue loading [23–26]. Fatigue striations are also observed as shown in Figure 10. Secondary cracking and crack branching has been observed in the cast MarBN at inclusions at the free surface and at subsurface locations (Figure 11). Figure 12 shows decohesion of the matrix from inclusions. EDX has been performed on these inclusions and the most common type identified in MarBN is a calcium-aluminium oxide. Other inclusion types identified, such as manganese sulphides, do not appear to promote fatigue cracking or matrix decohesion.

3.3. Material Modelling

The initial and optimised material parameters for MarBN at 600 °C are presented in Table 3. Figures 13 and 14 show the results of the optimisation process in terms of model fit to the experimental data for the initial cycle and half-life of MarBN at 600 °C, across a range of strain-rates and strain-ranges. Figures 15 and 16 show the comparison of the effect of strain-range on the predicted and measured damage evolutions for both MarBN and P91. Figure 17 demonstrates the effect of increasing cycles on the cyclic stress-strain loop as a result of cyclic softening and fatigue damage accumulation. Figure 18 shows the evolution of the maximum plastic strain for MarBN and P91 at 600 °C, with the model showing good agreement to the experimental data. Figure 19 presents a comparison of the predicted number of reversals to failure against the experimental data for all of the above cases.

4. Discussion

The HTLCF behaviour of a cast nano-strengthened martensitic steel, MarBN, has been characterised via a programme of strain-controlled cyclic tests covering different strain-rates and strain-ranges, including results at 600 °C and 650 °C. The characterisation includes measurement and numerical modelling of cyclic evolution of stresses, plastic strains, softening and fatigue damage, as well as microstructural analysis of the material and fractography of the post-test specimens. Furthermore, comparisons have been made with rolled P91 steel, the corresponding material currently used widely in industry.

At 600 °C, MarBN is seen to have a significantly higher strength than P91 (see also Barrett et al. [20]), prior to the onset of fatigue damage, which during which the microstructurally induced softening is replaced by fatigue induced damage (Figure 3(a)). This is a key benefit of MarBN for application to higher temperatures and pressures, compared to materials currently used in steam header applications for current generation fossil fuel power plants. Although MarBN has a much coarser grain structure, as illustrated in Figure 8, the increased strength (including cyclic) of MarBN at high temperature (compared to P91) is attributed to a more stable distribution of boron-enriched $M_{23}C_6$ carbides along grain and lath boundaries, in combination with a significant tungsten solid solution strengthening mechanism. Furthermore, a comparison of the microstructure of MarBN from

the as-received condition to post-test at 600 °C (Figure 8) indicates very little change in the block boundaries. However, in the context of the changing nature of power plant operation, it is important to note that cast MarBN also displays a significantly higher rate of softening than rolled P91. This will need to be considered in power plant design for flexible operation. At 650 °C, MarBN shows a strength which is comparable to P91 at 600 °C for early cycles, but more rapidly softens and displays a significantly shorter fatigue life. The lower fatigue performance of MarBN at 600 °C may simply be due to the cast nature of this particular MarBN product, compared to the rolled nature of the P91 tested here, e.g. see Williams et al. [42].

The presence of ductile dimples and fatigue striations on the fracture surface of MarBN are characteristic of fatigue failure in metals. Dimples on the fracture surface can occur due to microvoid coalescence and growth at defects, such as inclusions. These phenomena have been observed on the fracture surface of MarBN samples which have been tested at 600 °C as well as 650 °C, indicating the important mechanisms of deformation occurring during loading. Microvoid growth and coalescence is of particular importance as impurities have been identified as a key cause of failure, particularly when the impurity is located close to the surface [22–25], as has been observed in MarBN. The mechanical properties of inclusions differ from the matrix and there is generally a low-strength interface bond between inclusions and the matrix. Decohesion or inclusion fracture is found to primarily result from stress concentrations due to dislocation pile-ups at inclusions [21–23,41]. Microstructural analysis of MarBN indicates that fatigue failure may occur as a result of the presence of inclusions and increasing plastic deformation; however the role of dislocations must be quantified in more detail to fully characterise the mechanisms of deformation from the microscale. The presence of inclusions in metals under low-cycle fatigue loading has been found to seriously degrade the mechanical properties, with inclusions identified as crack initiation sites by multiple sources. The presence of calcium-aluminium oxides have been identified as key regions of crack initiation and propagation, and larger inclusion size is found to increase the fracture stress of the material [25,26,43].

The material parameter identification and optimisation procedure, outlined here with application to MarBN and P91 for high temperature cyclic behaviour and fatigue damage prediction, is shown to

provide excellent correlation with the measured failure lives across a range of strain-rates and strain-ranges. A key novel aspect of the present work, which has facilitated this excellent correlation, is the application of the Chaboche non-linear isotropic softening equation, with primary and secondary softening parameters (R_1 and R_2), in comparison to the measured softening behaviour, to demarcate the onset and evolution of fatigue damage-induced softening, characterised by the Z variable. However, the accuracy achieved in relation to numerical simulation of the evolving cyclic viscoplasticity behaviour of the material (Figures 13 and 14), preceding fatigue damage, is key to this demarcation process. Undoubtedly, future work should focus on the development of more physically-based models, such as the dislocation mechanics based approaches of Fournier et al. [44], Giroux et al. [45], and more recently, for cyclic behaviour of 9Cr steels, Barrett et al. [6]. Nonetheless, from a design perspective, the phenomenological constitutive modelling of the present work is ideal for rapid turnaround of results and simulation of complex geometries and loading conditions. However, again, the Coffin-Manson fatigue model used here has the advantage of facilitating expedient identification of parameters. Interestingly, a key ingredient in the success of the predictive method presented is the accurate prediction of evolving plastic strain range, which is central to the Coffin-Manson equation.

5. Conclusion

This paper presents experimental and constitutive modelling of the high temperature low-cycle fatigue behaviour of MarBN and P91, including life prediction and damage accumulation. Some key conclusions are:

- Mechanisms of deformation, characteristic of fatigue failure, have been identified at both 600 °C and 650 °C, indicating the importance of void growth and coalescence.
- Inclusions have been identified as a key cause of microvoid initiation and growth due to matrix decohesion. The presence of inclusions at the free surface provides sites for cracking and crack branching.
- A fatigue life and damage accumulation model is developed in conjunction with a hyperbolic sine unified cyclic viscoplasticity material model, which incorporates non-linear combined

isotropic softening and kinematic hardening. A key aspect of the model is the demarcation of fatigue damage from microstructure-induced softening via comparison of the non-linear isotropic evolution with the measured softening response.

- The new fatigue damage methodology is applied to MarBN at 600 °C and P91 at 500 °C and 600 °C. The results show excellent correlation of predicted and measured fatigue lives for different strain-rate and strain-range conditions.
- Further uniaxial and multiaxial experimental testing in conjunction with microstructural analysis (e.g. transmission electron microscopy) is necessary to fully characterise the fatigue and stress relaxation behaviour, as well as the key micro- and nano-mechanisms of deformation in the material.

Acknowledgments

The authors wish to acknowledge funding from the Irish Research Council and GE Power under the Enterprise Partnership Scheme (EPSPG/2015/55). The authors would also like to express their gratitude to Mr. Rod Vanstone from GE Power, and Dr. Barry O'Brien and Mr. Conor O'Hagan from NUI Galway. The authors acknowledge the facilities and technical assistance of the NCBES Electron Microscopy unit within the Centre for Microscopy & Imaging at the National University of Ireland Galway, a facility that is funded by NUIG and the Irish Government's Programme for Research in Third Level Institutions, Cycles 4 and 5, National Development Plan 2007-2013. The authors would like to acknowledge the contributions made by the collaborators of the MECHANNICS project, including Mr. S. Scully and Ms. Adelina Adams of ESB Energy International. The author's would also like to acknowledge the contributions made by the IMPEL group, including Dr. David Allen of IMPACT Power Ltd., Dr. Craig Degnan of E.ON New Build and Technology, Dr. Peter Barnard and Dr. Paul Moody of Doosan Power, Mr. Steve Roberts and Mr. Ryan Leese of Goodwin Steel Castings, and Prof. Rachel Thomson and Dr. Mark Jepson of Loughborough University.

References

[1] R. Viswanathan, K. Coleman, U. Rao, Materials for ultra-supercritical coal-fired power plant boilers, Int. J. Press. Vessel. Pip. 83 (2006) 778–783.

[2] F. Masuyama, History of power plants and progress in heat resistant steels, ISIJ Int. 41 (2001) 612–625.

[3] G. Golański, J. Kępa, The effect of ageing temperatures on microstructure and mechanical properties of GX12CrMoVNbN9-1 (GP91) cast steel, Arch. Metall. Mater. 57 (2012) 575–582. doi:10.2478/v10172-012-0061-0.

[4] T.P. Farragher, S. Scully, N.P. O'Dowd, S.B. Leen, Thermomechanical analysis of a pressurized pipe under plant conditions, J. Press. Vessel Technol. 135 (2013) 11204.

[5] T.P. Farragher, S. Scully, N.P. O'Dowd, S.B. Leen, Development of life assessment procedures for power plant headers operated under flexible loading scenarios, Int. J. Fatigue. 49 (2013) 50–61.

[6] R.A. Barrett, P.E. O'Donoghue, S.B. Leen, A dislocation-based model for high temperature cyclic viscoplasticity of 9–12Cr steels, Comp. Mater. Sci. 92 (2014) 286–297.

[7] R.A. Barrett, P.E. O'Donoghue, S.B. Leen, An improved unified viscoplastic constitutive model for strain-rate sensitivity in high temperature fatigue, Int. J. Fatigue. 48 (2013) 192–204.

[8] S. Mroziński, G. Golański, A. Zielińska-Lipiec, Fatigue resistance of GX12CrMoVNbN9-1 cast steel after ageing process, Mater. Sci. 20 (2014) 396–402.

[9] R.A. Barrett, T.P. Farragher, C.J. Hyde, N.P. O'Dowd, P.E. O'Donoghue, S.B. Leen, A unified viscoplastic model for high temperature low cycle fatigue of service-aged P91 steel, J. Press. Vessel Technol. 136 (2014) 21402.

[10] F. Abe, Precipitate design for creep strengthening of 9% Cr tempered martensitic steel for ultra-supercritical power plants, Sci. Technol. Adv. Mater. 9 (2008) 13002.

[11] R.A. Barrett, Experimental Characterisation and Computational Constitutive Modelling of High Temperature Degradation in 9Cr Steels Including Microstructural Effects, PhD Thesis, National University of Ireland Galway, 2016.

[12] K. Maruyama, K. Sawada, J. Koike, Strengthening mechanisms of creep resistant tempered martensitic steel, ISIJ Int. 41 (2001) 641–653.

[13] L. Li, R. MacLachlan, M.A.E. Jepson, R. Thomson, Microstructural evolution of boron nitride particles in advanced 9Cr power plant steels, Metall. Mater. Trans. A. 44 (2013) 3411–3418.

[14] S.K. Albert, M. Kondo, M. Tabuchi, F. Yin, K. Sawada, F. Abe, Improving the creep properties of 9Cr-3W-3Co-NbV steels and their weld joints by the addition of boron, Metall. Mater. Trans. A. 36 (2005) 333–343.

[15] M. Tabuchi, M. Kondo, K. Kubo, S.K.S. Albert, Improvement of Type IV creep cracking resistance of 9Cr heat resisting steels by boron addition, OMNI. 3 (2004) 1–11. http://www.ommi.co.uk/PDF/Articles/99.pdf.

[16] J.S. Dubey, H. Chilukuru, J.K. Chakravartty, M. Schwienheer, A. Scholz, W. Blum, Effects of cyclic deformation on subgrain evolution and creep in 9–12% Cr-steels, Mater. Sci. Eng. A. 406 (2005) 152–159.

[17] T. Farragher, Thermomechanical Analysis of P91 Power Plant Components, PhD Thesis, National University of Ireland Galway, 2014.

[18] G. Golański, S. Mroziński, Fatigue life at 550°C temperature of aged martensitic cast steel, AASRI Procedia. 2 (2012) 249–255. doi:10.1016/j.aasri.2012.09.042.

[19] A.A. Saad, W. Sun, T.H. Hyde, D.W.J. Tanner, Cyclic softening behaviour of a P91 steel under low cycle fatigue at high temperature, Procedia Eng. 10 (2011) 1103–1108.

[20] R.A. Barrett, E.M. O'Hara, P.E. O'Donoghue, S.B. Leen, High-temperature low-cycle fatigue behavior of MarBN at 600 °C, J. Press. Vessel Technol. 138 (2016) 41401. http://dx.doi.org/10.1115/1.4031724.

[21] F. Abe, M. Tabuchi, H. Semba, M. Igarashi, M. Yoshizawa, N. Komai, A. Fujita, Feasibility of MARBN steel for application to thick section boiler components in USC power plant at 650 C, in: Proc. 5th Int. Conf. Adv. Mater. Technol. Foss. Power Plants, Oct., 2007: pp. 3–5.

[22] F. Ellyin, Fatigue Damage, Crack Growth and Life Prediction, Springer Science & Business Media, 2012.

[23] S. Murakami, Continuum Damage Mechanics: A Continuum Mechanics Approach to the Analysis of Damage and Fracture, Springer Science & Business Media, 2012.

[24] F.C. Campbell, Fatigue and Fracture: Understanding the Basics, ASM International, 2012.

[25] X. Xie, L. Zhang, M. Zhang, J. Dong, K. Bain, Micro-mechanical behavior study of non-metallic inclusions in P/M disk superalloy Rene'95, Superalloys. (2004) 451–458.

[26] D. Hull, Fractography: Observing, Measuring and Interpreting Fracture Surface Topography, Cambridge University Press, 1999.

[27] S. Suresh, Fatigue of Materials, Cambridge University Press, 1998. doi:10.1017/CBO9780511806575.

[28] L.M. Kachanov, Time of the rupture process under creep conditions, Izv Akad Nauk S S R Otd Tech Nauk. 8 (1958) 26–31. doi:citeulike-article-id:5466815.

[29] Y. Rabotnov, Creep Rupture, Springer, Berlin, 1968.

[30] J. Lemaitre, R. Desmorat, Engineering Damage Mechanics: Ductile, Creep, Fatigue and Brittle Failures, Springer Science & Business Media, 2005.

[31] J.L. Chaboche, P.M. Lesne, A non-linear continuous fatigue damage model, Fatigue Fract. Eng. Mater. Struct. 11 (1988) 1–17.

[32] K. Golos, F. Ellyin, A total strain energy density theory for cumulative fatigue damage, J. Press. Vessel Technol. 110 (1988) 36–41. doi:10.1115/1.3226012.

[33] G. Cheng, A. Plumtree, A fatigue damage accumulation model based on continuum damage mechanics and ductility exhaustion, Int. J. Fatigue. 20 (1998) 495–501.

[34] R.W. Neu, H. Sehitoglu, Thermomechanical fatigue, oxidation, and creep: Part II. Life prediction, Metall. Trans. A. 20 (1989) 1769–1783. doi:10.1007/BF02663208.

[35] J. Shang, T.H. Hyde, S.B. Leen, Finite element-based life prediction for high-temperature cyclic loading of a large superplastic forming die, 41 (2006) 539–559. doi:10.1243/03093247JSA236.

[36] S.-P. Zhu, H.-Z. Huang, Y. Liu, R. Yuan, L. He, An efficient life prediction methodology for low cycle fatigue–creep based on ductility exhaustion theory, Int. J. Damage Mech. (2012) 1056789512456030.

[37] W.Z. Wang Buhl, P., Klenk, A, A unified viscoplastic constitutive model with damage for multi-axial creep–fatigue loading, Int. J. Damage Mech. 24 (2015) 363–382. doi:10.1177/1056789514537007.

[38] L.F. Coffin, Fatigue at high temperature, in: Fatigue Elev. Temp., ASTM International, 1973.

[39] Private Communication, IMPEL Consortium, 2015.

[40] J.L. Chaboche, G. Rousselier, On the plastic and viscoplastic constitutive equations—Part I: Rules developed with internal variable concept, J. Press. Vessel Technol. 105 (1983) 153–158.

[41] J.-L. Chaboche, G. Rousselier, On the plastic and viscoplastic constitutive equations—Part II: application of internal variable concepts to the 316 stainless steel, J. Press. Vessel Technol. 105 (1983) 159–164.

[42] J. Williams, A. Fatemi, Fatigue performance of forged steel and ductile cast iron crankshafts, SAE Technical Paper, 2007.

[43] W.W. Bose Filho, A.L.M. Carvalho, P. Bowen, Micromechanisms of cleavage fracture initiation from inclusions in ferritic welds. Part I. Quantification of local fracture behaviour observed in notched testpieces, Mater. Sci. Eng. A. 460-461 (2007) 436–452. doi:10.1016/j.msea.2007.01.115.

[44] B. Fournier, M. Sauzay, A. Pineau, Micromechanical model of the high temperature cyclic behavior of 9-12%Cr martensitic steels, Int. J. Plast. 27 (2011) 1803–1816. doi:10.1016/j.ijplas.2011.05.007.

[45] P.F. Giroux, F. Dalle, M. Sauzay, C. Caës, B. Fournier, T. Morgeneyer, A.F. Gourgues-Lorenzon, Influence of strain rate on P92 microstructural stability during fatigue tests at high temperature, Procedia Eng. 2 (2010) 2141–2150. doi:10.1016/j.proeng.2010.03.230.

Tables

Table 1. Experimental high temperature test program for MarBN.

Test Type	*Strain-range (%)*	*Strain-rate (%/s)*	*Waveform*
HTLCF 600 °C	±0.5	0.1	R_ε = -1 (Triangular)
	±0.5	0.033	
	±0.4	0.033	
	±0.3	0.033	
	±0.5	0.01	
	±0.4	0.01	
	±0.3	0.01	
HTLCF 650 °C	±0.5	0.1	R_ε = -1 (Triangular)
Cyclic Dwell 600 °C	±0.5	0.1	1 hour hold period

Table 2. Coffin-Manson and Damage constants for MarBN at 600 °C and P91 at 500 °C and 600 °C.

Material	*Temp (°C)*	ε_f' *(-)*	*c (-)*	ϕ_1	ϕ_2
MarBN	600	0.42	-0.68	0.79	15.41
P91	500	0.35	-0.59	0.80	29.23
P91	600	4.97	-0.92	0.85	18.52

Table 3. Material parameters for MarBN at 600 °C and P91 at 500 °C and 600 °C.

	E (GPa)	*k (MPa)*	Q_1 *(MPa)*	b_1 *(-)*	Q_2 *(MPa)*	b_2 *(-)*	C_1 *(MPa)*	γ_1 *(-)*	C_2 *(MPa)*	γ_2 *(-)*	α (s^{-1})	β (MPa^{-1})
MarBN (Initial)	162	100.0	-74.14	5.90	-73.81	0.25	296,262	5,492.1	61,574.3	601.9	2.0×10^{-6}	0.031
MarBN (Optimised)	162	100.5	-68.35	11.11	-70.88	0.41	296,256	5,610.1	61,545.7	626.3	9.1×10^{-7}	0.035
P91 (500 °C)	173	121.04	-46.67	2.00	-52.11	0.13	304,370	3,422.5	48,484.5	406.7	8.0×10^{-7}	0.055
P91 (600 °C)	144	54.04	-72.90	3.02	-52.11	0.13	275,130	3,397.2	38,101.2	626.6	9.0×10^{-7}	0.055

Figures

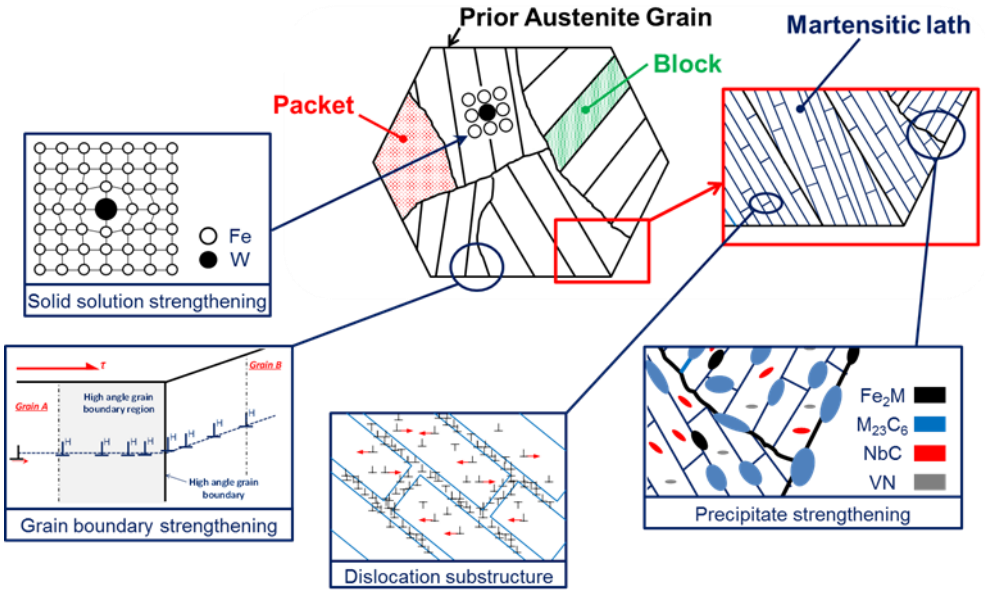

Figure 1. Hierarchical microstructure of 9Cr martensitic steels, with the primary strengthening mechanisms identified [11].

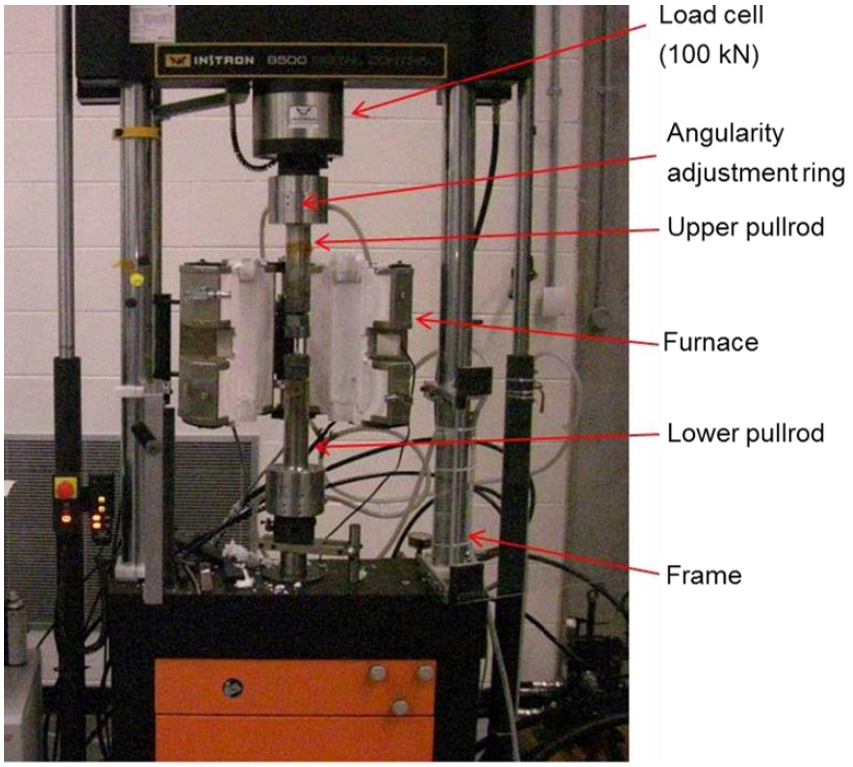

Figure 2. INSTRON 8500 test rig at NUI Galway, for strain-controlled high temperature testing.

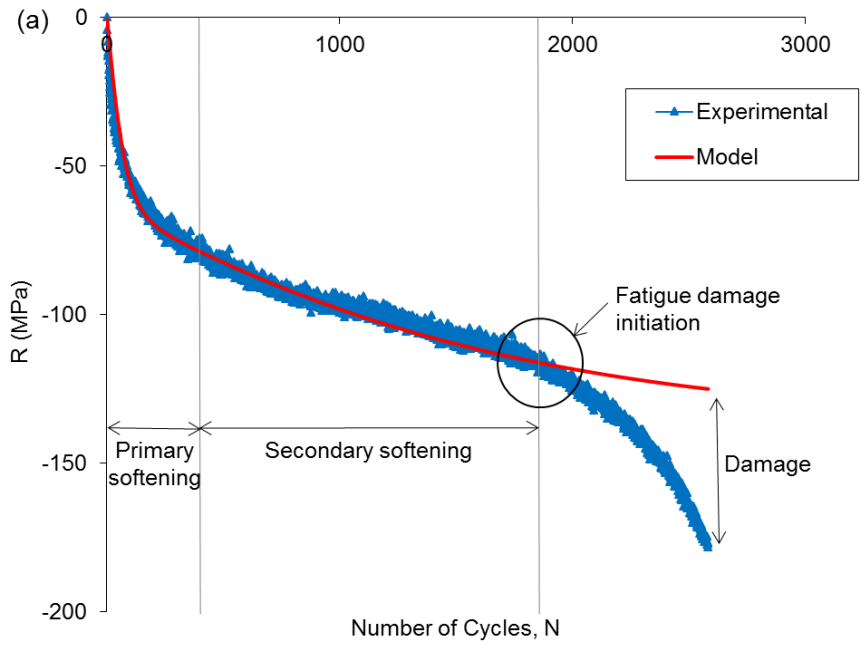

1

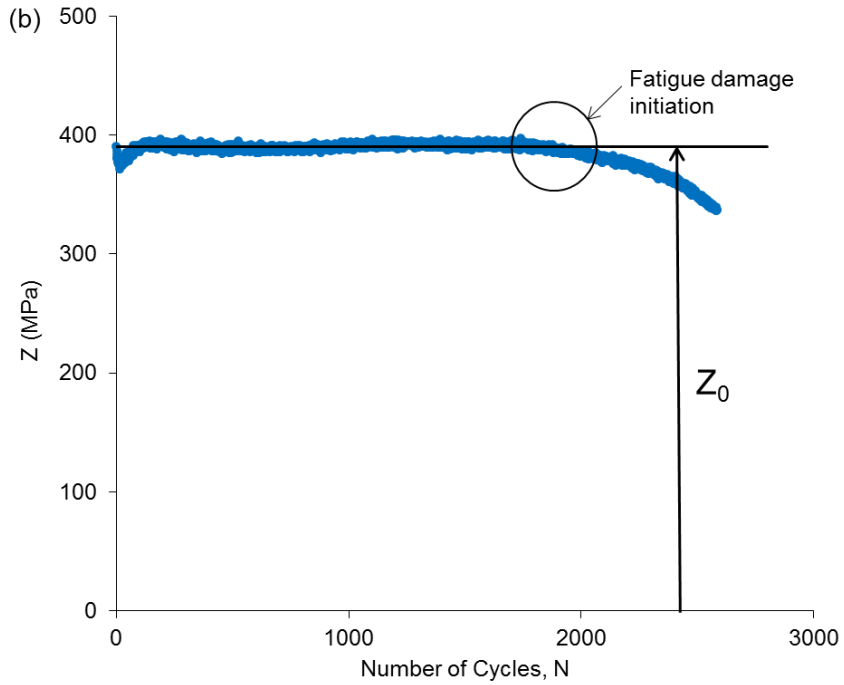

2

3 *Figure 3. (a) Comparison of the model to experimental data for MarBN at 600 °C and (b) identification of Z_0 value.*

4

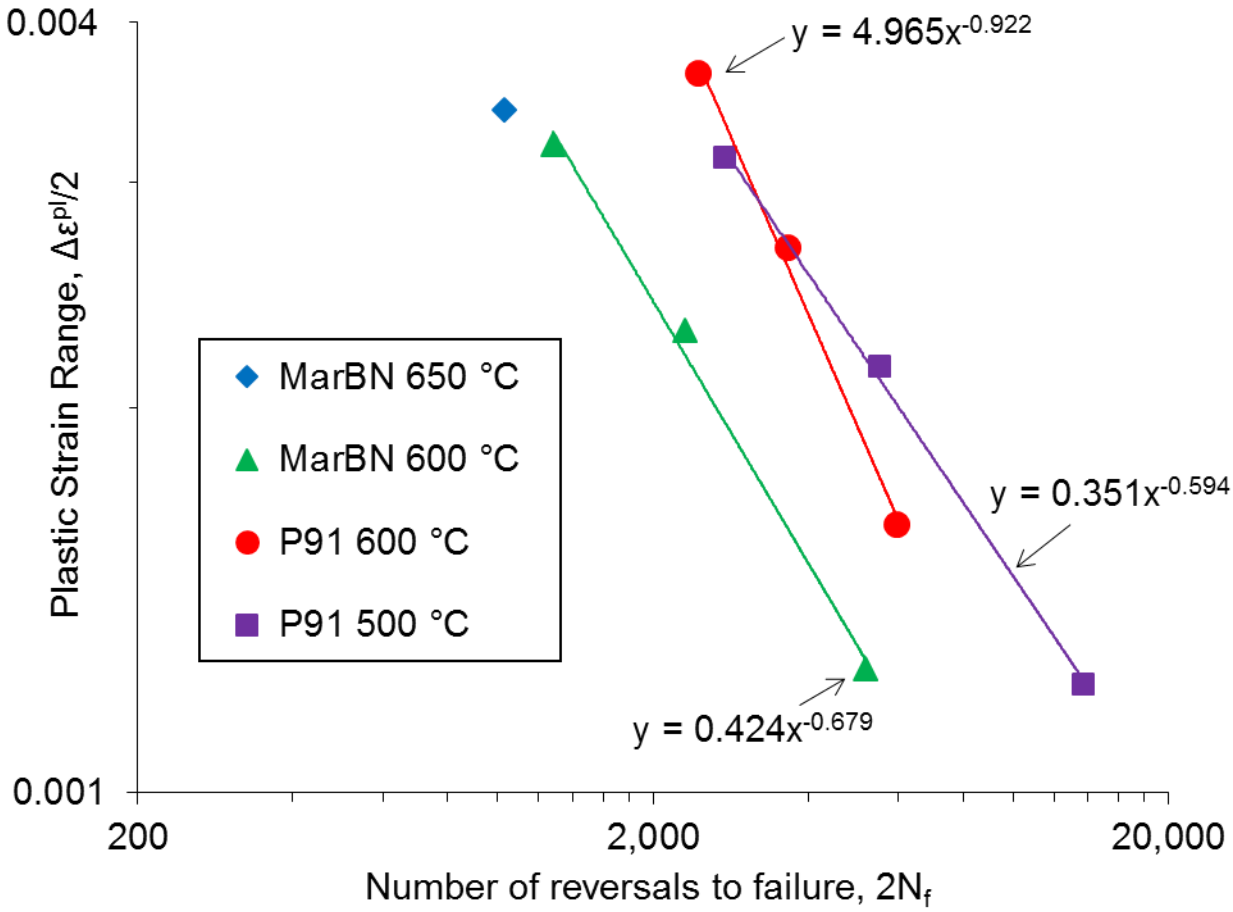

Figure 4. Identification of Coffin-Manson constants for MarBN and P91.

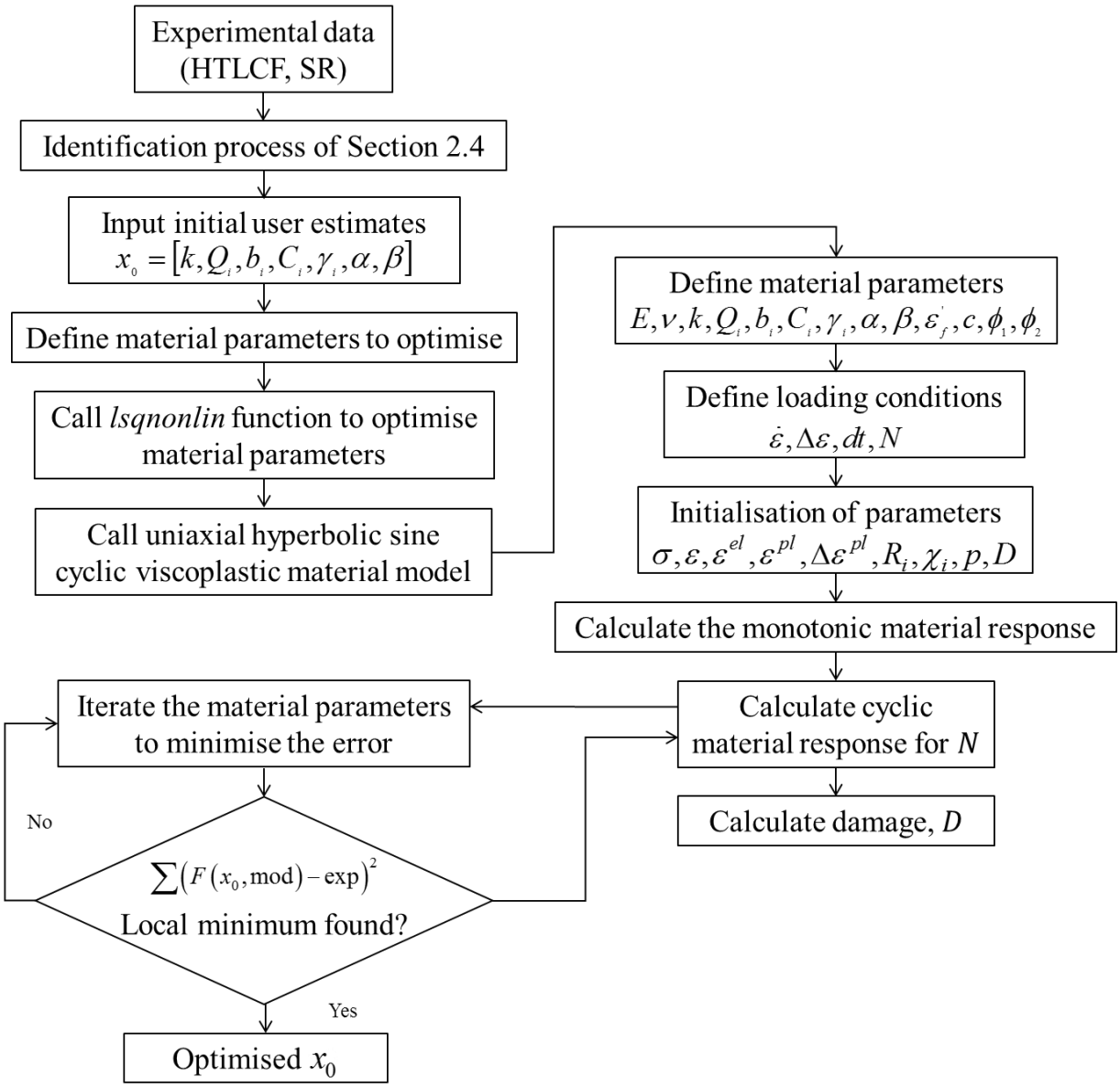

Figure 5. Flowchart of the material parameter optimisation process, in conjunction with the uniaxial hyperbolic sine cyclic viscoplastic material model, applied to the MarBN material parameters.

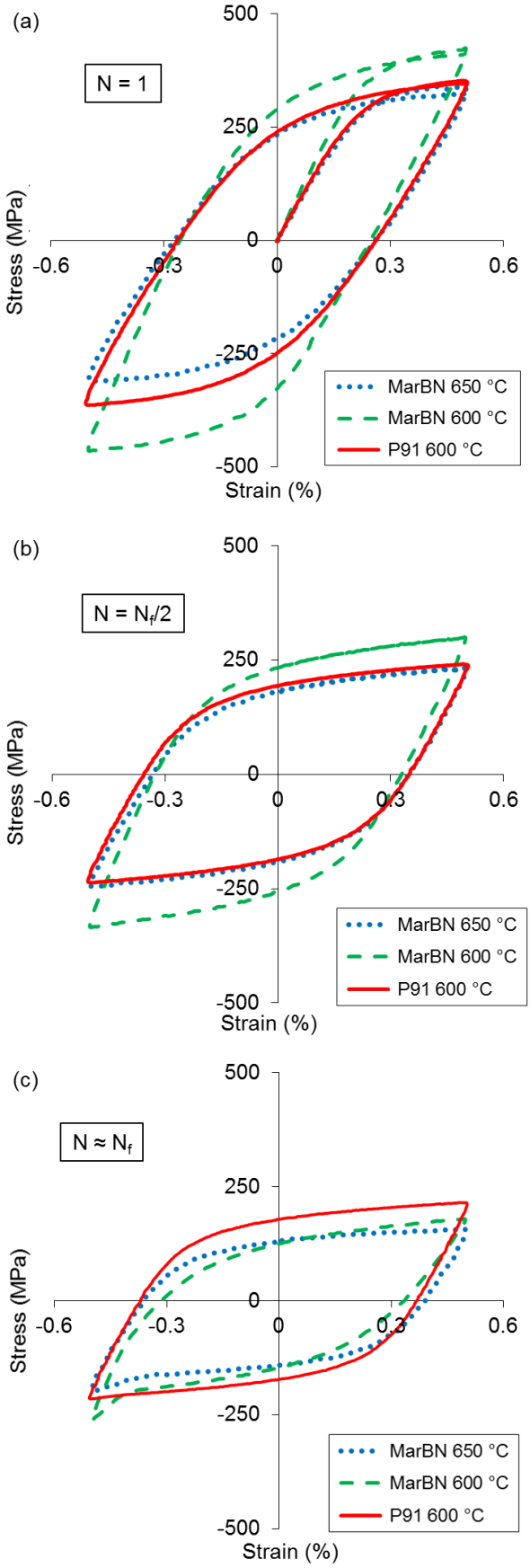

Figure 6. Comparison of the fatigue response of MarBN at 600 °C and 650 °C and P91 at 600 °C, at a strain-rate of 0.1 %/s and applied strain-range of ±0.5% for the (a) initial cycle, (b) half-life and (c) approximate final cycle.

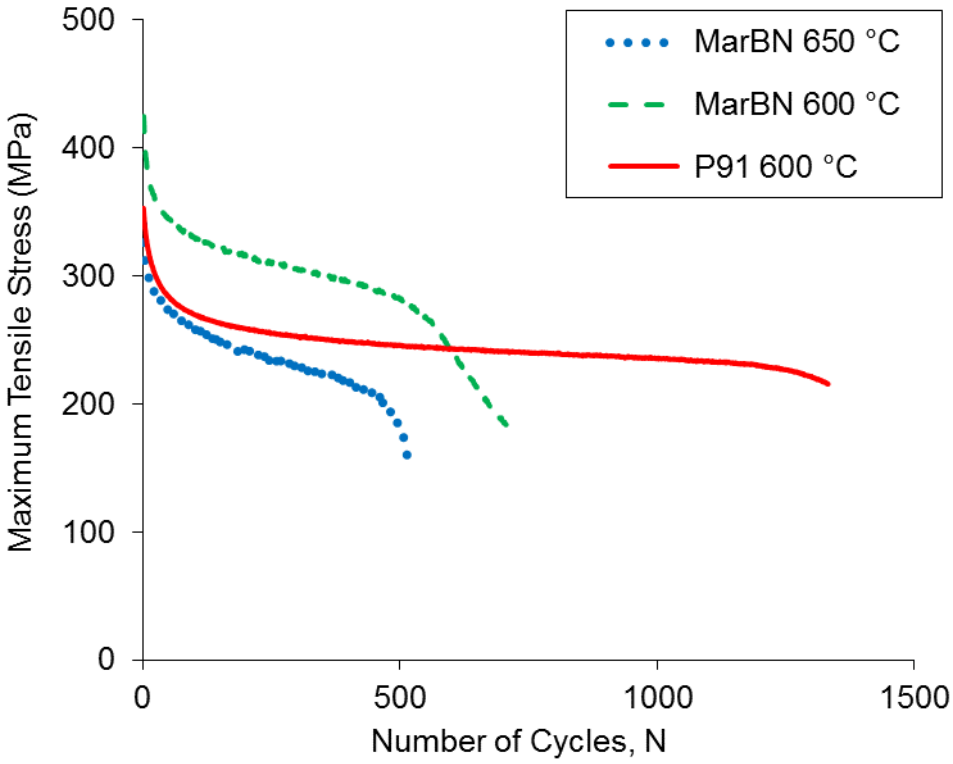

Figure 7. Cyclic softening in MarBN at 600 °C and 650 °C, compared to P91 at 600 °C.

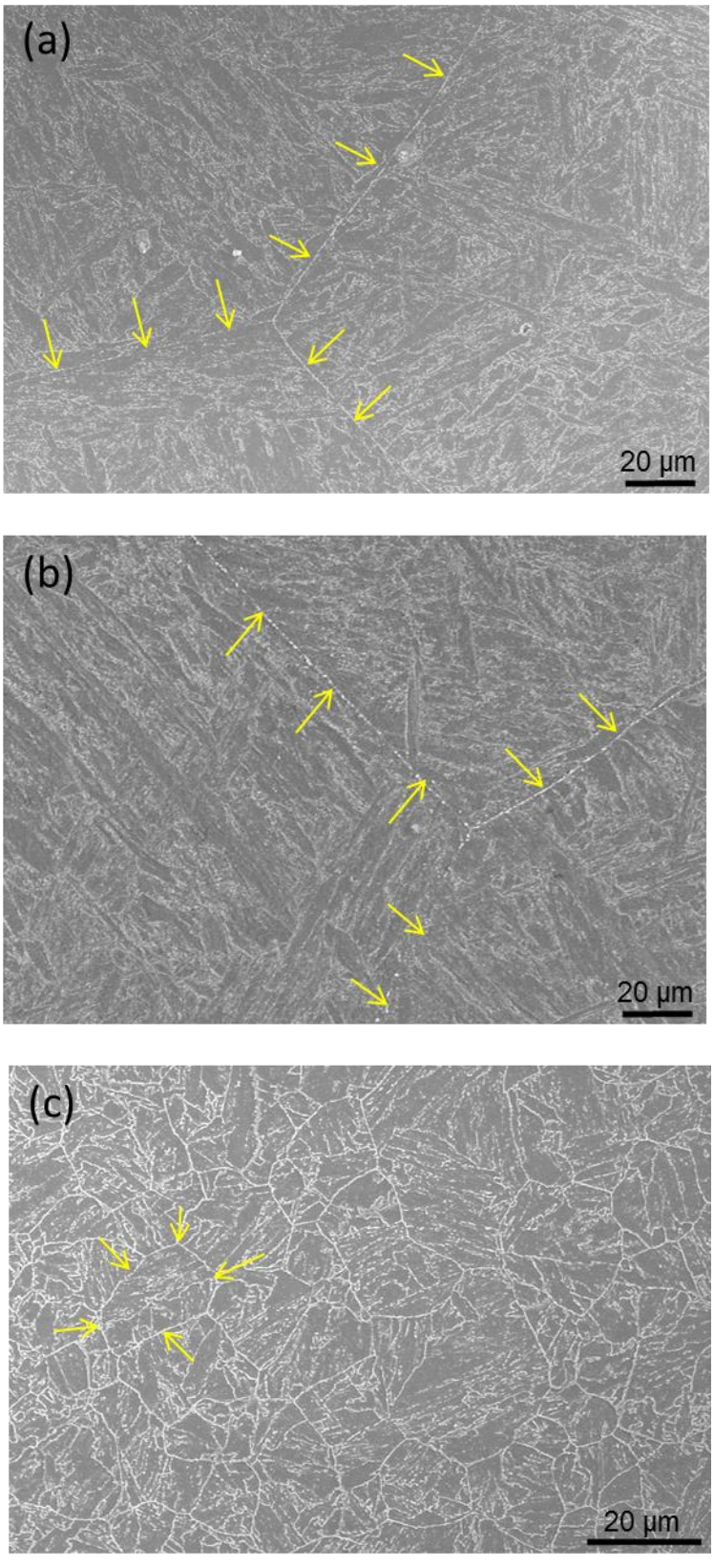

Figure 8. SEM images of the microstructure of (a) as-received MarBN, (b) MarBN post-HTLCF test at 600 °C and (c) P91 post-HTLCF test at 600 °C, with grain boundaries (yellow arrows) highlighted.

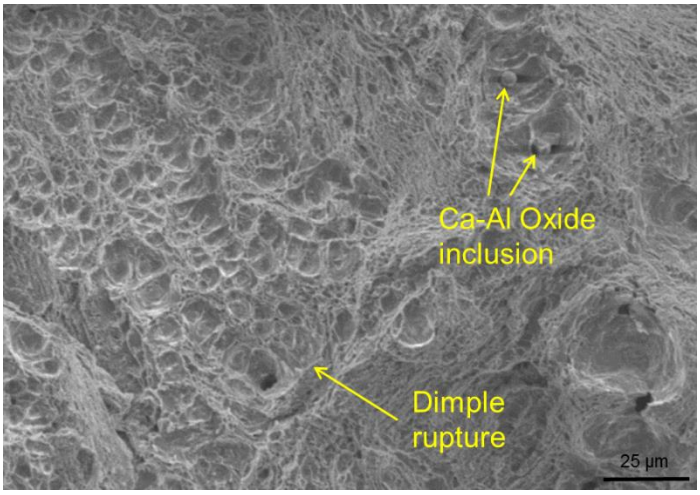

Figure 9. Ductile dimple rupture, with Ca-Al Oxide inclusions, on the fracture surface of MarBN at 650 °C.

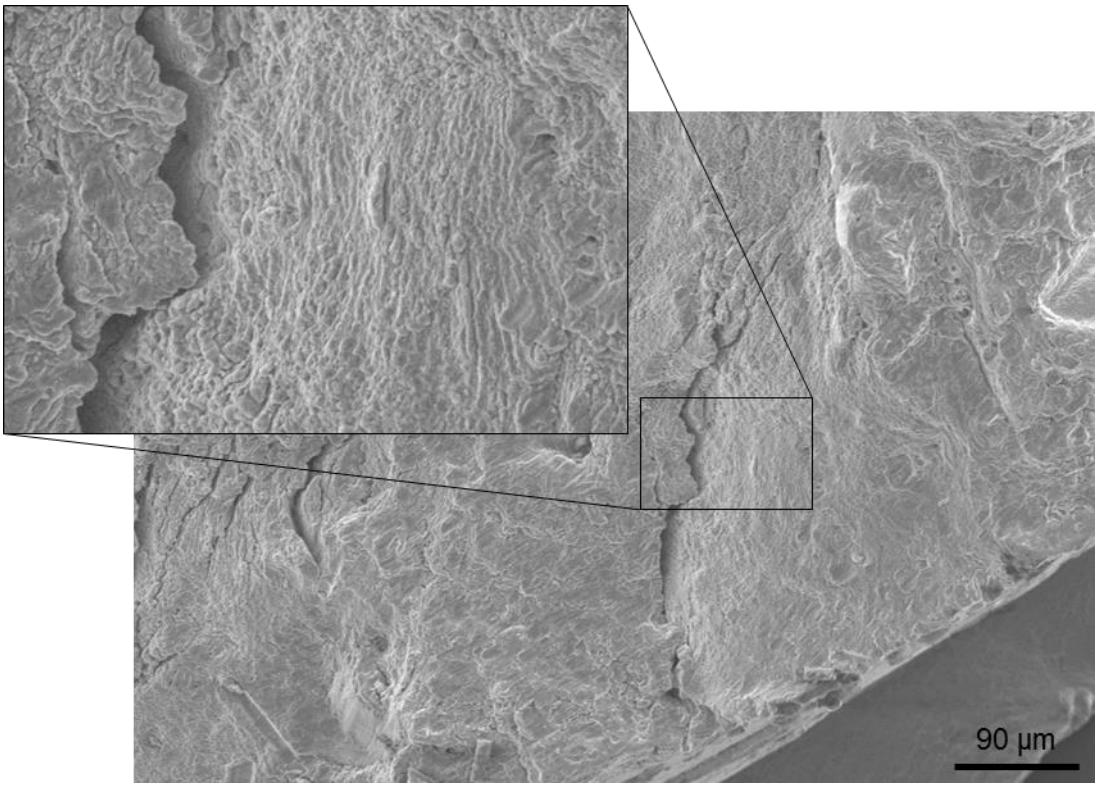

Figure 10. Fatigue striations parallel to a crack in MarBN post-HTLCF test at 650 °C.

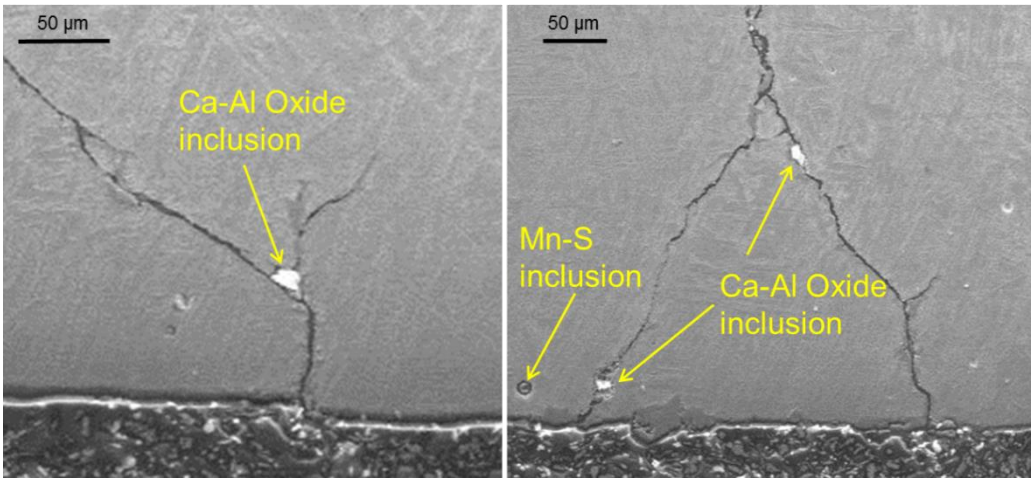

Figure 11. Ca-Al Oxide inclusions at regions of secondary cracking along the gauge length of MarBN with a Mn-S inclusion post-HTLCF test at 600 °C.

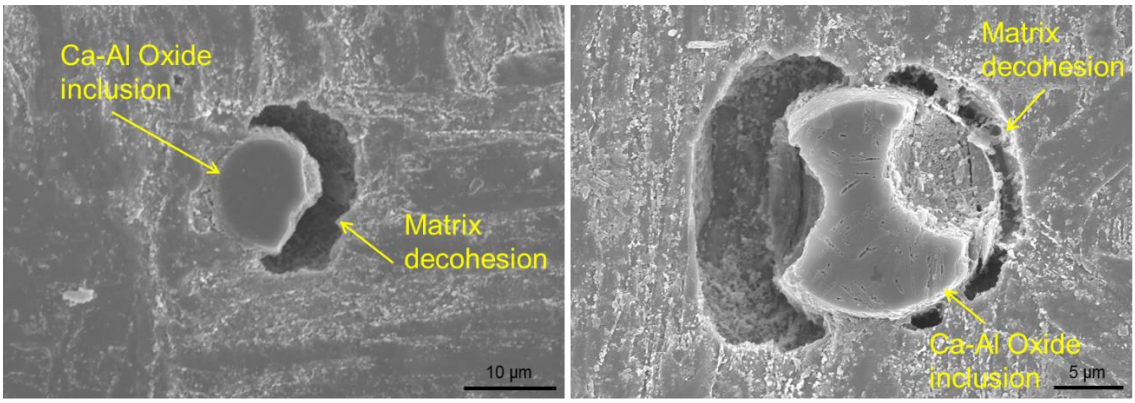

Figure 12. Matrix decohesion at Ca-Al Oxide inclusions in MarBN post-HTLCF testing at 650 °C.

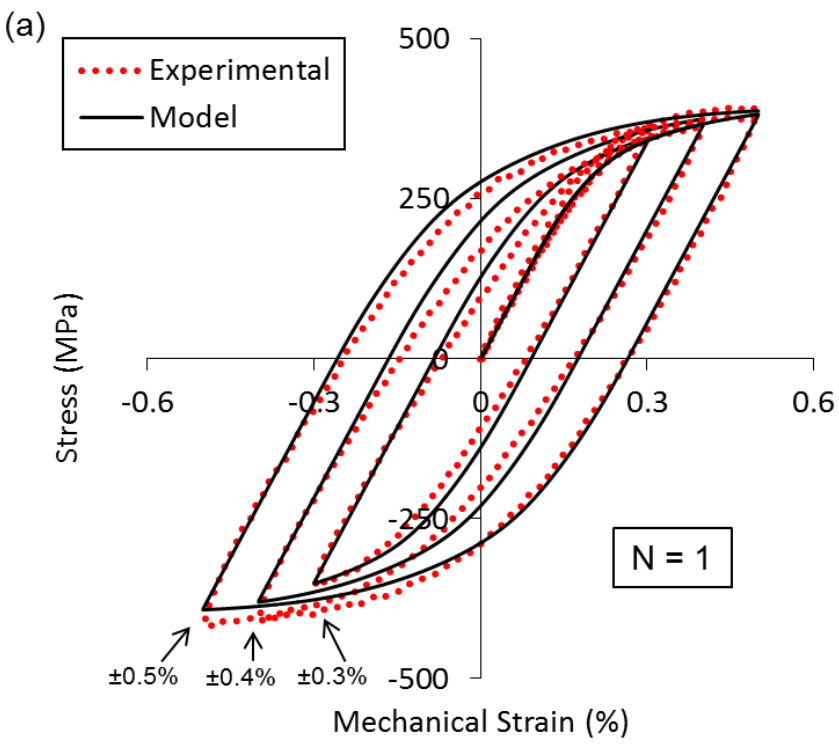

1

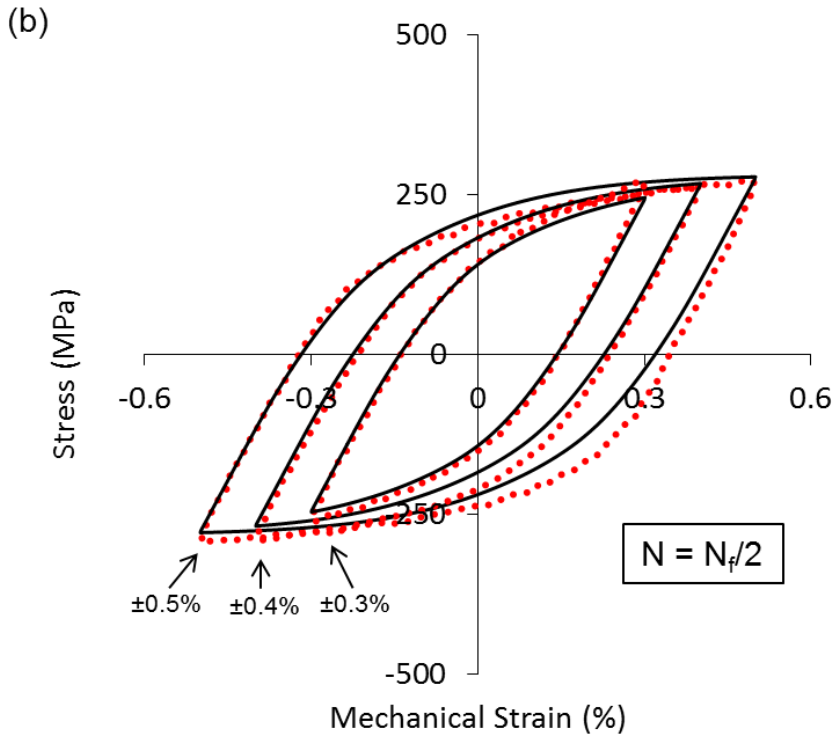

2

3 *Figure 13. Comparison of the model to experimental data for MarBN at 600 °C at a strain-rate of 0.01 %/s, for the (a)*
4 *initial cycle and (b) half-life.*

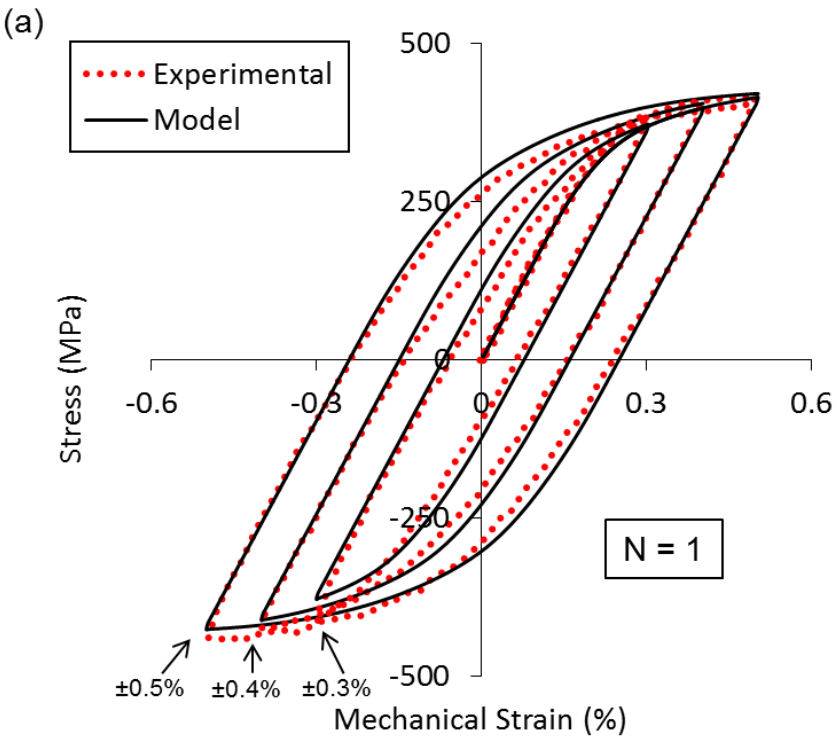

1

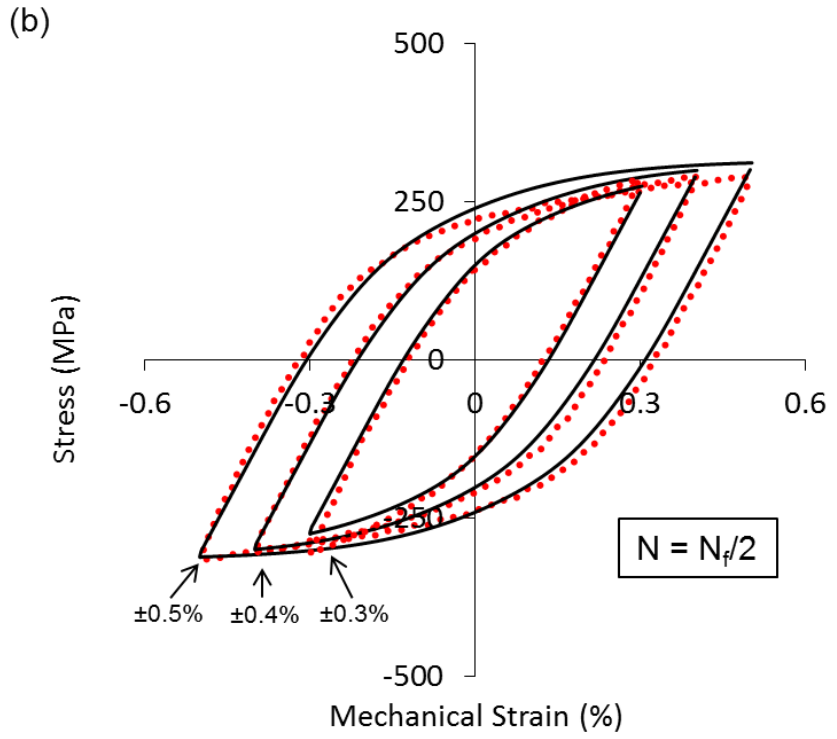

2

3 *Figure 14. Comparison of the model to experimental data for MarBN at 600 °C at a strain-rate of 0.033 %/s, for the (a)*
4 *initial cycle and (b) half-life.*

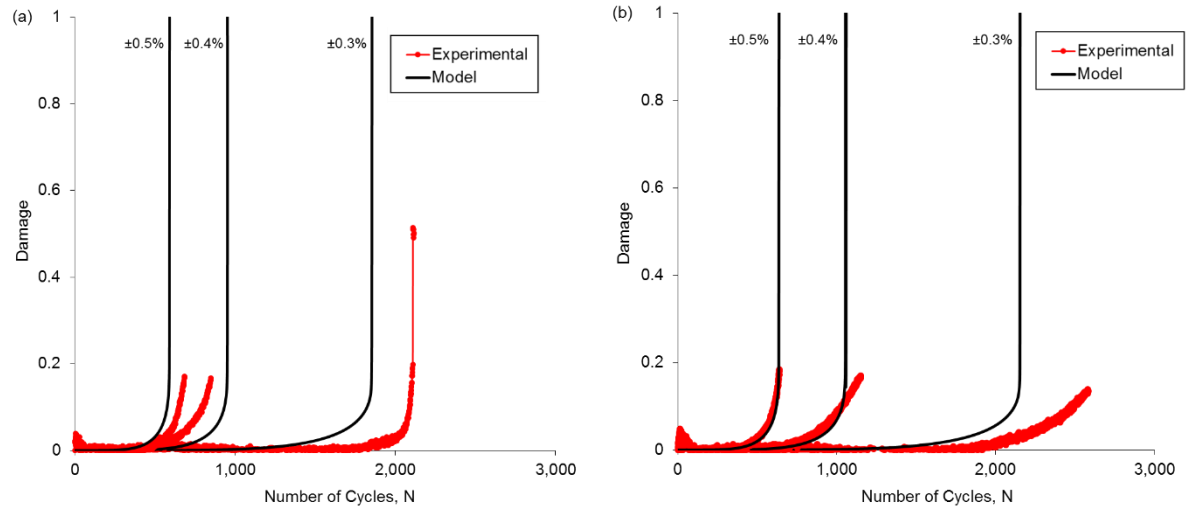

Figure 15. Comparison of effect of strain-range on predicted and measured damage evolutions for MarBN at 600 °C for strain-rates of (a) 0.01 %/s and (b) 0.033 %/s.

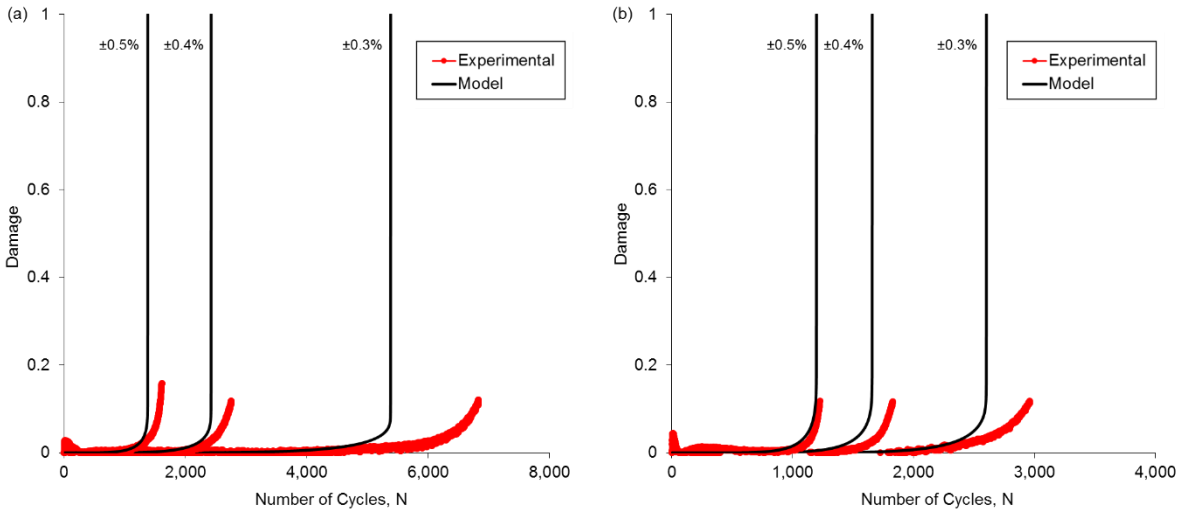

Figure 16. Comparison of effect of strain-range on predicted and measured damage evolutions for P91 at a strain-rate of 0.033 %/s and temperature of (a) 500 °C and (b) 600 °C.

.

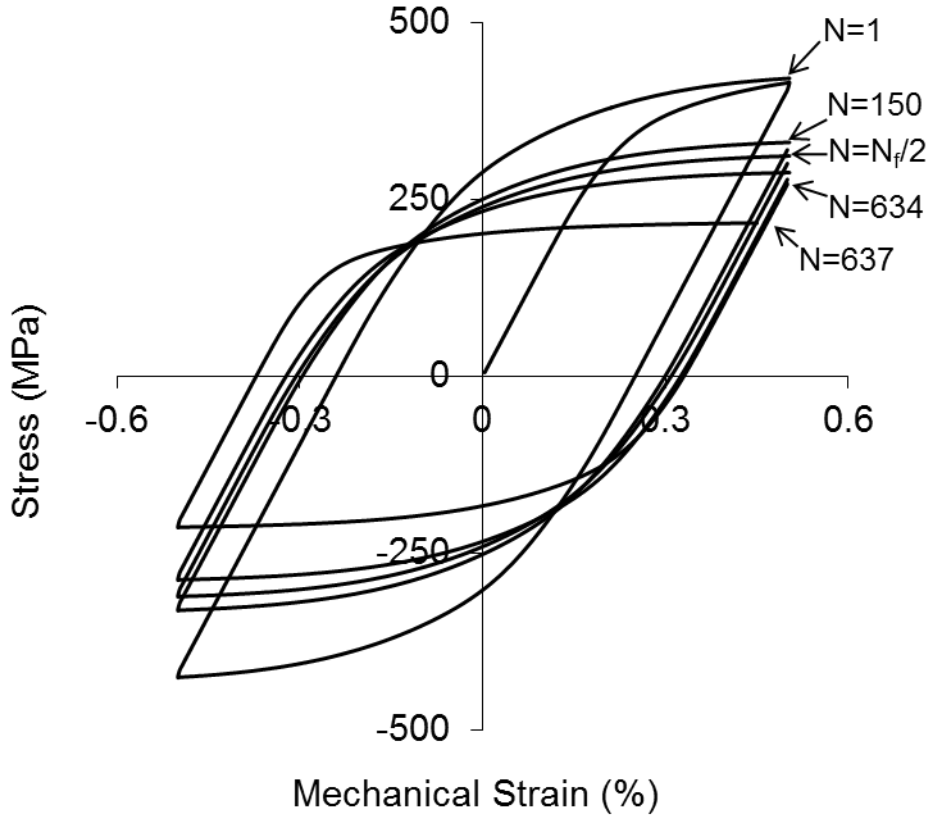

Figure 17. Material modelling of MarBN at 600 °C for a strain-rate of 0.033 %/s demonstrating the effects of damage on the cyclic stress-strain loop

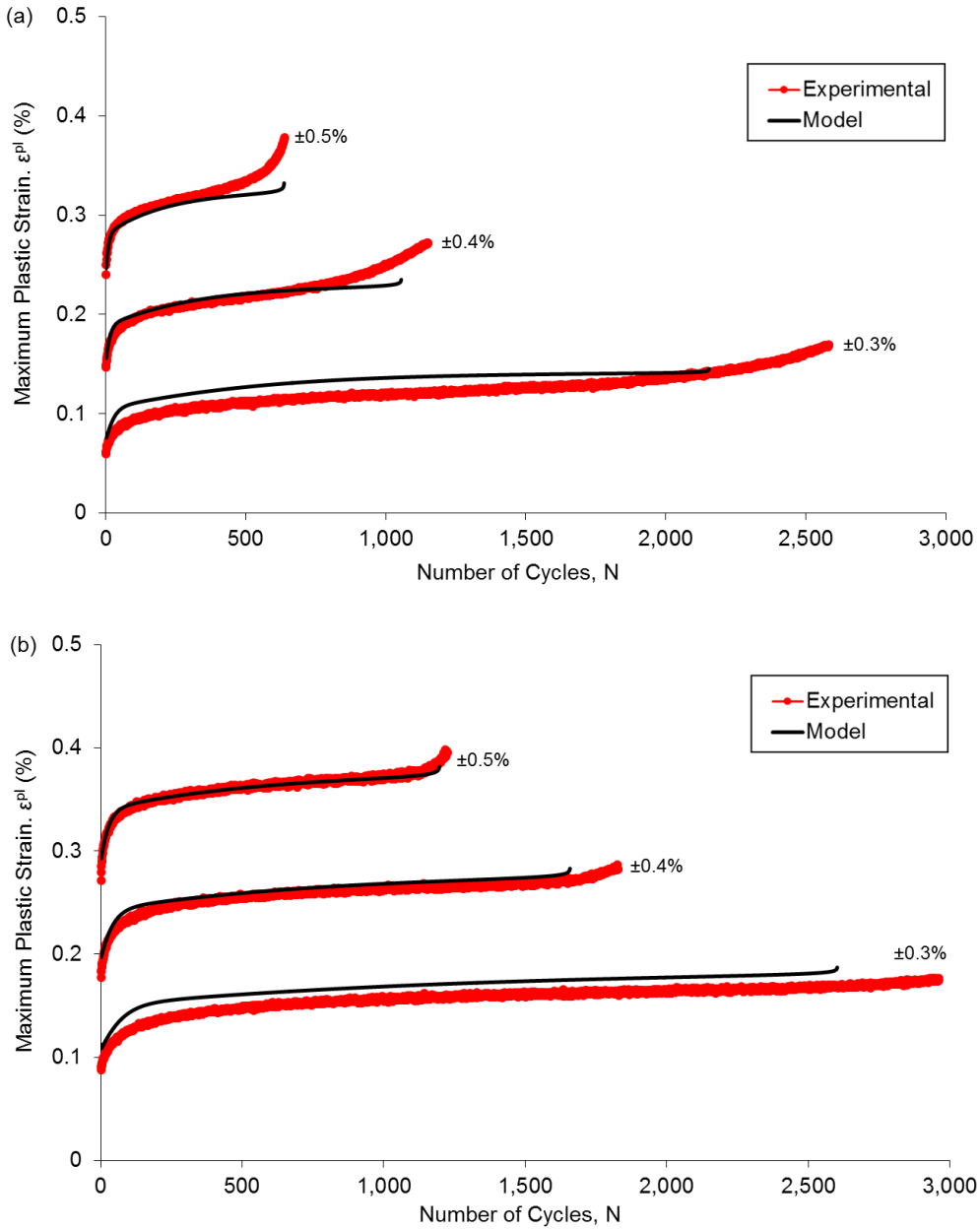

Figure 18. Comparison of the predicted and measured maximum plastic strain in (a) MarBN at 600 °C at a strain-rate of 0.033 %/s and (b) P91 at 600 °C at a strain-rate of 0.033 %/s .

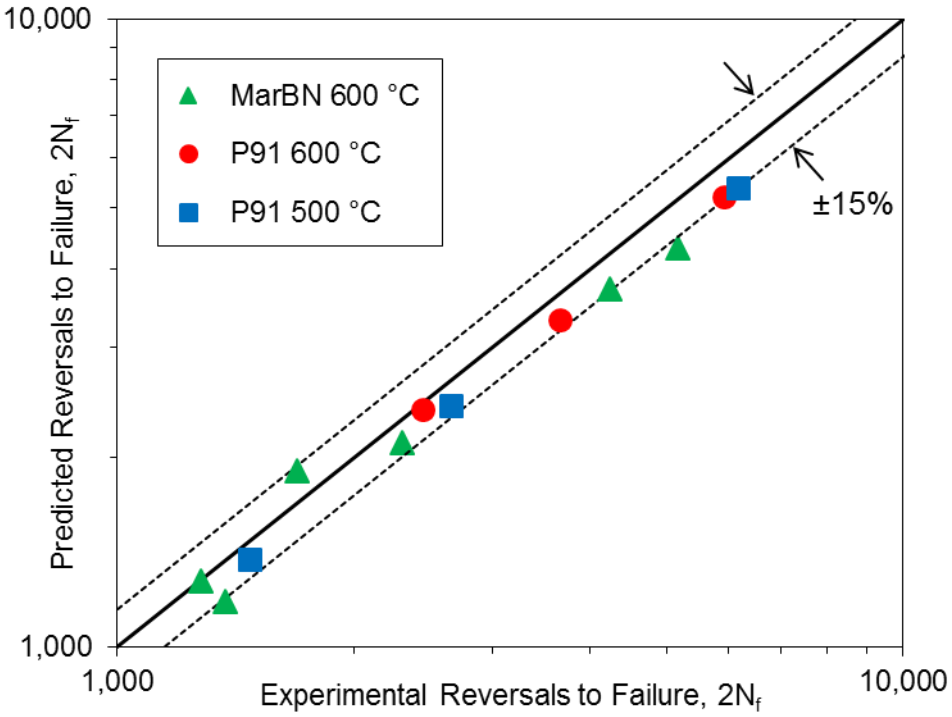

Figure 19. Comparison of the predicted and experimental number of reversals to failure for MarBN at 600 °C and P91 at 500 °C and 600 °C.